

Avian-Inspired Claws Enable Robot Perching and Walking

Mohammad Askari^{1*}, Won Dong Shin^{1†}, Damian Lenherr¹, William Stewart^{2†}, *Member, IEEE*, and Dario Floreano¹, *Fellow, IEEE*

Abstract—Multimodal UAVs (Unmanned Aerial Vehicles) are rarely capable of more than two modalities, i.e., flying and walking or flying and perching. However, being able to fly, perch, and walk could further improve their usefulness by expanding their operating envelope. For instance, an aerial robot could fly a long distance, perch in a high place to survey the surroundings, then walk to avoid obstacles that could potentially inhibit flight. Birds are capable of these three tasks, and so offer a practical example of how a robot might be developed to do the same. In this paper, we present a specialized avian-inspired claw design to enable UAVs to passively perch and walk. The key innovation is the combination of a Hoberman linkage leg with Fin Ray[®] claw that uses the weight of the UAV to wrap the claw around a perch, or hyperextend it in the opposite direction to form a ball shape for stable terrestrial locomotion. Because the design uses the weight of the vehicle, the underactuated design is lightweight and low power. With the inclusion of talons, the 45 g claws are capable of holding a 700 g UAV to an almost 20-degree angle on a perch. In scenarios where cluttered environments impede flight and long mission times are required, such a combination of flying, perching, and walking is critical.

Index Terms—Bio-Inspired Robots, Perching Claw, Multimodal Locomotion, Compliant Mechanism, Unmanned Aerial Vehicle.

I. INTRODUCTION

RECENTLY, there has been a lot of interest in perching UAVs (Unmanned Aerial Vehicles). The advantages of perching include being able to use less energy than when maintaining flight, having the opportunity to recharge or refuel, and enabling long-term surveillance. Studies on UAV-perching have usually considered only flying and landing [1]–[12], and more rarely, retakeoff [13]–[16]. However, once landed, it may be necessary for the robot to move around to complete its mission. While in many cases the UAV could just take off and fly to its next location, this is not always possible. In such a case, the combination of flying, perching, and legged locomotion would be helpful. Many birds are capable of all these abilities [17], [18] and therefore provide great examples of how robots could do the same.

Robotic flying-walking hybrid locomotion has been shown to be feasible on flat obstacle-free ground [19]. DUCK consisted of a multicopter with legs that could walk on the

ground, take off, land, and fly repeatedly, but could not perch. One recent demonstration by another robot, LEONARDO, was dexterous enough to ‘slackline’ [20]. This robot used simple feet combined with active control from the quadcopter motors for balance and disturbance rejection. As a result, it requires constant power to remain in one spot. For search and rescue missions, robots could be required to hold position for long periods of time, acting as communication relays or fixed sensors for hours at a time, which would require heavy batteries. Having a way to combine aerial-legged multimodality with passive perching could enable robots to operate for much longer periods of time compared to fully actuated robots of similar mass.

In this article, we focus on leg and claw design to imbue a flying robot with the ability to passively perch and walk. Inspired by the feet of birds, we propose a novel Fin Ray[®] [21] claw design for a UAV that can passively perch on a horizontal pole and walk on the ground (Fig. 1). When the weight of the UAV presses on it, the claw passively wraps around and holds the perch. The weight is removed from the claw at takeoff, allowing it to slip off the perch. The claw can be switched to a hyperextended state, in which the weight of the UAV instead causes the claw to curl upward. This can then enable the vehicle to walk around. We characterize the limits of the passive perching, showing that a 700 g UAV can lean at 19.4 degrees before it slips. When in hyperextended mode, the ball-shaped claw provides a large support polygon, which enables a stable gait that is not possible with a claw that can only curl around an object to perch. We also measure the squeezing force of the claw under similar conditions and find that it can squeeze with a force up to its body weight. For comparison, birds can squeeze with a force of up to two times their body weight but rely on muscles to achieve that performance [18].

II. RELATED WORK

There are several examples of aerial-ground hybrid locomotion. These include a squirrel-inspired robot that can glide in the air, land, and then crawl under obstacles [22]; a winged UAV with rotating winglets that can push itself along the ground after landing [23]; A winged robot that uses mini-whisks to run on the ground [24]. Others implemented a round cage to allow them to roll around the ground [25]. For simplicity, some aerial-ground vehicles just use wheels [26]. However, due to the nature of these modes of ground locomotion, the above examples often have a hard time overcoming obstacles.

The most widely used foot designs in legged robots are ball-shaped feet and flat feet [27]. Ball-shaped feet do not limit the orientation of the feet with respect to the ground [27], but they

This work was supported by the Swiss National Science Foundation through the National Centre of Competence in Research (NCCR) and the European Union’s Horizon 2020 research and innovation program under grant agreement ID: 871479 AERIAL-CORE.

¹Mohammad Askari, Won Dong Shin, Damian Lenherr, and Dario Floreano are with the Laboratory of Intelligent Systems, École Polytechnique Fédérale de Lausanne (EPFL), CH-1015 Lausanne, Switzerland.

²William Stewart was with the Laboratory of Intelligent Systems, École Polytechnique Fédérale de Lausanne (EPFL), CH-1015 Lausanne, Switzerland. He is now with the Soft Flyers Group, Stony Brook University, 11794, New York, USA.

[†]These authors contributed equally to this work.

*Corresponding author: mohammad.askari@epfl.ch



Fig. 1. Sample mission of a flying-perching-walking robot for search and rescue. The inset views show comparisons of the feet of a purple finch and the robotic equivalent in different configurations. Photo credits: Rejean Aline; Claude Laprise; Olga Pink - Adobe Stock.

suffer from a limited contact area. This makes them ineffective at exerting a moment on the ground. On the other hand, flat feet provide a wide contact area but are limited in foot orientation. Ball-shaped feet are generally used in robots with four or more legs where using a moment with the ground is not as important as freedom of orientation. Flat feet are used in robots with one or two legs and are used to balance in moments when standing still. However, both these foot designs are only used for legged locomotion and not for grasping, perching, or other purposes.

If we turn to nature, we can see that birds are quite adept at perching, walking, and flying. Roderick et al. showed that when perching, Pacific Parrotlets use both friction between the pads of their feet in addition to talons to grip the perch [18]. Furthermore, they found that depending on the perch material and diameter, the relative importance of the talons or pads of their feet changes. In some cases, the force due to the talons can reach up to eight times that of the pads of their feet.

For many years, it was believed that birds utilize passive mechanisms to hold onto perches for long periods of time or while sleeping [28]. The basis of this hypothesis was a passive mechanism in the birds' claw consisting of tendons that pass behind the ankle and are pulled when the birds squat. This would enable birds to remain perched when resting or even sleeping. However, Galton et al. cast doubt on this theory using experimental data showing that European Starlings could adapt to surgically severed tendons and sleep on perches [29]. They also found that when anesthetized, the birds would fall from perches, which would not happen if there was a passive mechanism for perching. Nonetheless, many research groups have developed quadrotor perching mechanisms based on the incorrect tendon notion [1], [30], indicating that the mechanism could be useful even if birds are not utilizing it.

The mechanisms designed by these groups use stiff link segments (phalanges) connected by flexible joints [1], [30]. The tendon is an inelastic cable that transmits the weight of the vehicle into the phalanges, providing the actuation force. These underactuated designs allow the individual fingers to passively conform around objects of different shapes. The two designs in [1], [30] differ in the path of the tendon. As an

alternative to using tendons to achieve passive perching, other authors [31] used a slider mechanism in combination with Fin Ray[®] [21] digits in an opposing arrangement [31] that wrap around convex structure. Indeed, Fin Ray[®] fingers are also used in many compliant grippers [31]–[36]. Under load, the Fin Ray[®] finger structure bends in the opposite direction of the applied force and thus conform to the object. In the perching mechanism developed by Chi et al., digits were equipped with aluminum talons at the extremities of the Fin Ray[®] structure [31]. The weight of the vehicle would close the Fin Ray[®] digits and press the talons into the perch. A similar active Fin Ray[®] claw has been developed for flapping wing MAVs, which weighs only 45g [37]. This claw was shown to be effective on a variety of different-shaped perches, on slanted perches, and when approaching the perch from an angle. It is, however, quite limited in that any deviation from perfectly vertical perching after landing would cause the claw to fail.

Another approach to passive perching is the Sarrus mechanism [38], where the weight of the UAV causes hinged plates to fold on themselves. These closing hinges are rigidly connected to plates such that when they close, the plates are brought together, squeezing the perch. At takeoff, the body weight is lifted off the mechanism, allowing the hinged plates to open and passively release the perch. While the plates are effective at transmitting the forces to the perch, the robot is likely to slip when leaning over. This perching mechanism does not use tendons to transfer forces.

To date, none of the claws developed for perching have been used also for walking. Indeed, many of these passive claws only actuate themselves to curl around an object, which would inhibit walking performance. The leg and claw design described here leverages the weight of the vehicle for passive perching, but also enables inclined stable perch, and most importantly allows the flying vehicle to walk on the ground.

III. LEG AND CLAW DESIGN

The mechanical design combines a Hoberman linkage [39] leg with a Fin Ray[®] claw. The combined structure has two stable configurations, perched and hyperextended. In the

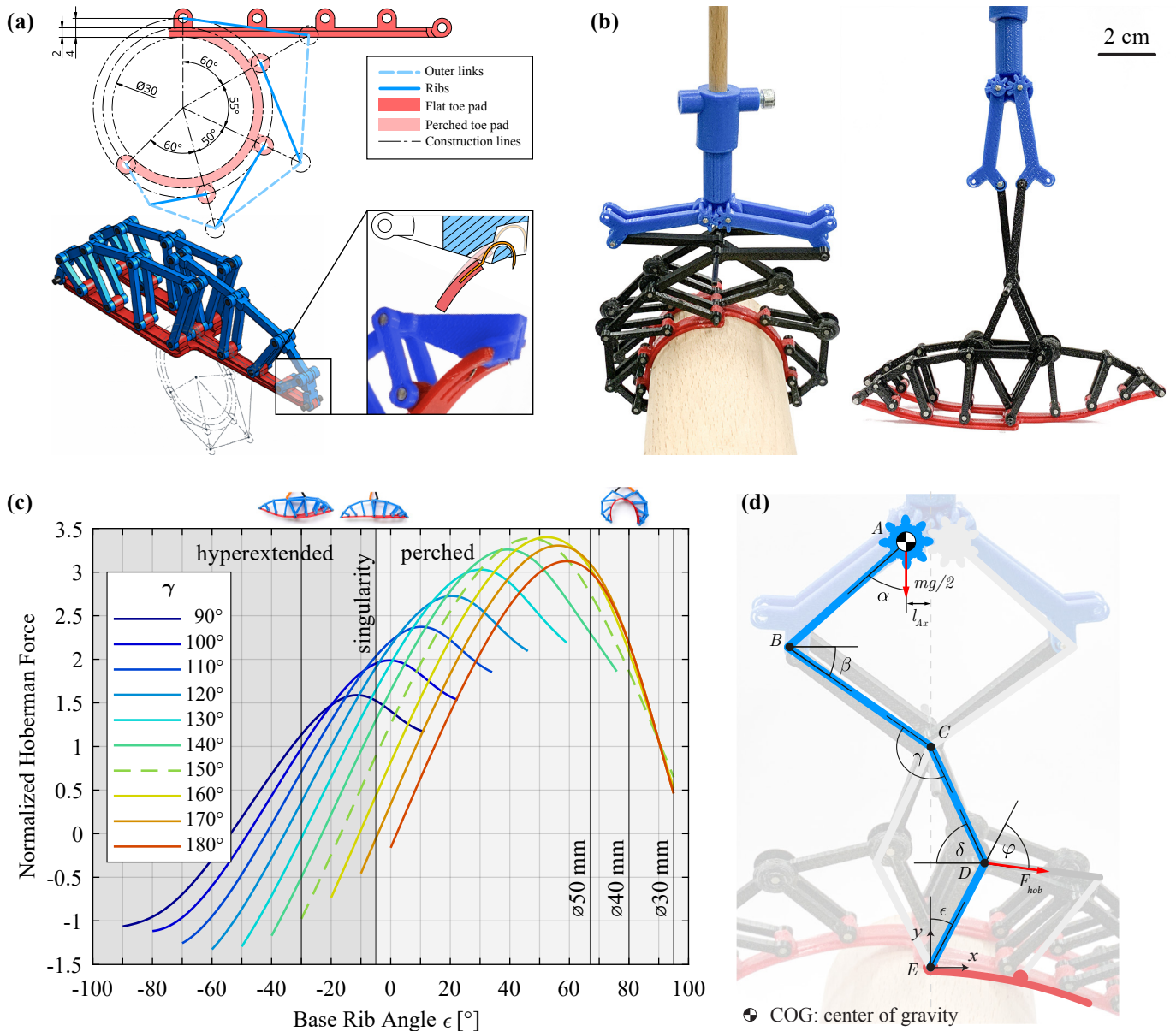


Fig. 2. Leg and claw design. (a) Geometric parameter sizing of the claw is done in the perched configuration, as shown in the top diagram. The CAD of the claw, comprising two front and one back digit with integrated talons, was sized based on the calculations presented in the bottom diagram. (b) Photos of the assembled claw in perched (left) and hyperextended (right) modes. (c) Mechanical advantage profiles of the Hoberman linkage over a range of base rib angles (ϵ) for different γ values. The two different shadings show whether the claw is within the perched or the hyperextended region. The vertical black line at -5 degrees indicates the singularity point where the claw switches between the two modes. The one at -30 degrees shows the limit of hyperextension reached passively for the selected claw geometry ($\gamma = 150^\circ$). The three other vertical black lines indicate the ϵ values for three different perch diameters, 30 mm, 40 mm, and 50 mm. (d) Diagram and geometric parameters of the linkage.

perched configuration, the Fin Ray[®] claw is curled inward, and in the hyperextended configuration, the claw is stretched out. We switch between perched and hyperextended modes by positioning the Hoberman linkage leg in a collapsed (perched) or stretched form (hyperextended), respectively. When moving from one configuration to another, the Fin Ray[®] claw passes through a singular point resembling a nearly flat claw. The moment the claw passes this singularity, the weight of the UAV will passively push the claw to either configuration.

The claw's design is inspired by the anisodactyl toe arrangement found in perching birds, where three digits (toes) face forward and one backward. To simplify the design, our claw

uses only two front digits. The palm of the claw is made of a flexible, 3D-printed TPU (Thermoplastic Polyurethane) toe pad (red in Fig. 2a). The ribs, 3D-printed in ABS (Acrylonitrile Butadiene Styrene), connect the upper surface of the toe pad to the outer-links of the Fin Ray[®] mechanism (blue structure in Fig. 2a). To increase perching stability, the claw includes talons (curved hooks) integrated at both extremities of the rib structure (inset of Fig. 2a). When a horizontal force is applied to the top of the central rib of each digit, the Fin Ray[®] ribs and outer-links transfer the loads along the digit, causing the digit to curl. Depending on the direction of the horizontal force, the digits will either curl down and close on a perch or stretch up

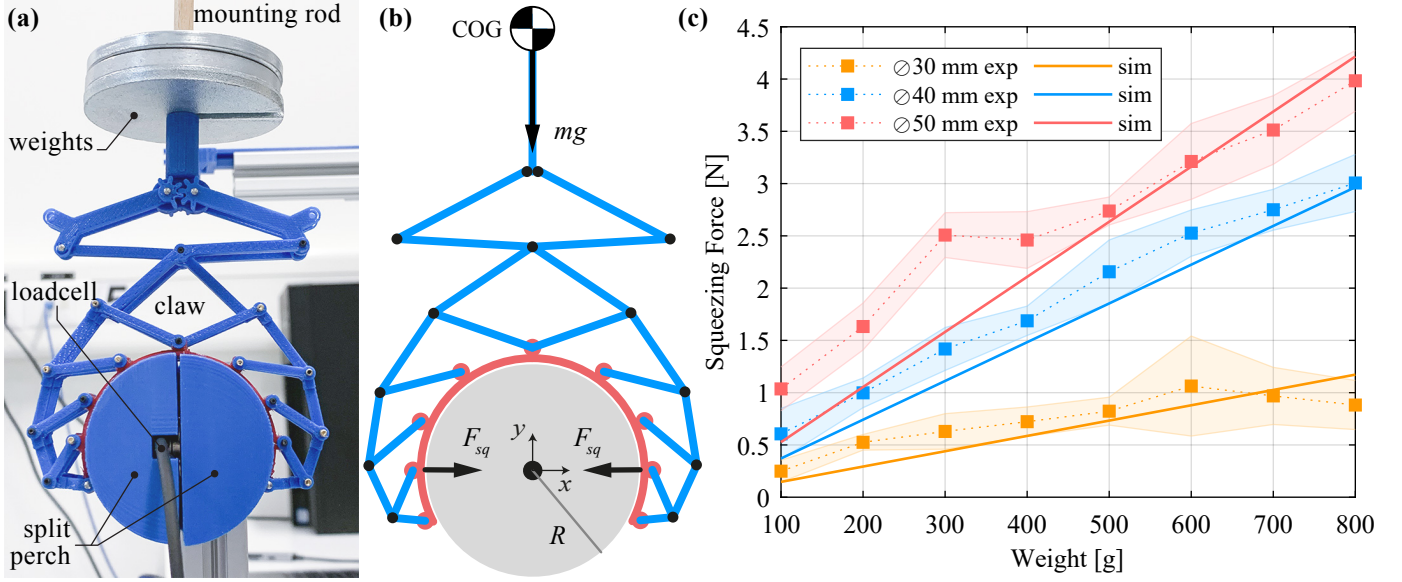


Fig. 3. (a) Image of the split perch experimental setup. Two halves of the split perch, 3D-printed in ABS, encompass the ATI Nano17 loadcell. Weights are mounted to a wooden rod, which press on the talon-less claw, which transforms the weight into a squeezing force, which in turn is measured by the loadcell. (b) Diagram of the claw in perched configuration. A static model is developed to approximate the squeezing force (see Supplementary Text for more details). (c) Plot of the estimated and measured squeezing force as a function of weight. Experiments are done for three different perch diameters with weights corresponding to different possible vehicle weights in steps of 100 g. The shaded regions represent the standard deviation of 10 measurements.

into a hyperextended mode creating a foot shape suitable for walking (left and right respectively in Fig. 2b).

The geometry of the Hoberman linkage regulates the curling angle of the Fin Ray[®] claw. In particular, the angle of the linkage (γ in Fig. 2d) affects the magnitude of the Hoberman force and the resulting curling angle of the claw (F_{hob} and ϵ in Fig. 2d, respectively). The output force imparted on the Fin Ray[®] claw by the weight of the UAV can be modeled with:

$$F_{hob} = \frac{\sin \epsilon + \cos \epsilon \left(\frac{l_{BC}}{l_{CD}} \left(\frac{\cos \beta}{\sin \delta} + \tan \alpha \frac{\sin \beta}{\sin \delta} \right) + \frac{\cos \delta}{\sin \delta} \right)}{\sin \phi} mg/2, \quad (1)$$

where AB, BCD, and DE are the individual links and α , β , γ , δ , ϵ , and ϕ are the corresponding angles (Fig. 2d). The two most critical angles are γ and ϵ , and the rest are geometrically dependent on these two. This is because γ is set when designing the claw and does not vary, and ϵ is a direct measure of how far the claw can curl or stretch. Using equation 1, we calculated F_{hob} for a variety of γ and ϵ values. γ was varied between 90 and 180 degrees in increments of 10 degrees. A γ value of 150 degrees was selected for the claws developed in this work. (Fig. 2c). This is because, at 150 degrees, the claw balances an ability to reach the hyperextended state (dashed line at $\epsilon = -30$ degrees in Fig. 2c) as well as being able to curl around a perch of 30 mm diameter (dashed line at $\epsilon = -95$ degrees in Fig. 2c). In addition, the maximum achievable Hoberman Force occurs at $\gamma = 150$ degrees. Changing γ shifts the achievable range of ϵ values. For example, increasing γ would allow the claw to reach a higher maximum ϵ , which corresponds to being able to perch on smaller diameter perches (This corresponds to the right end of the red $\gamma = 180$ degrees line in Fig. 2c being at $\epsilon = 95$ degrees whereas the right end of the blue

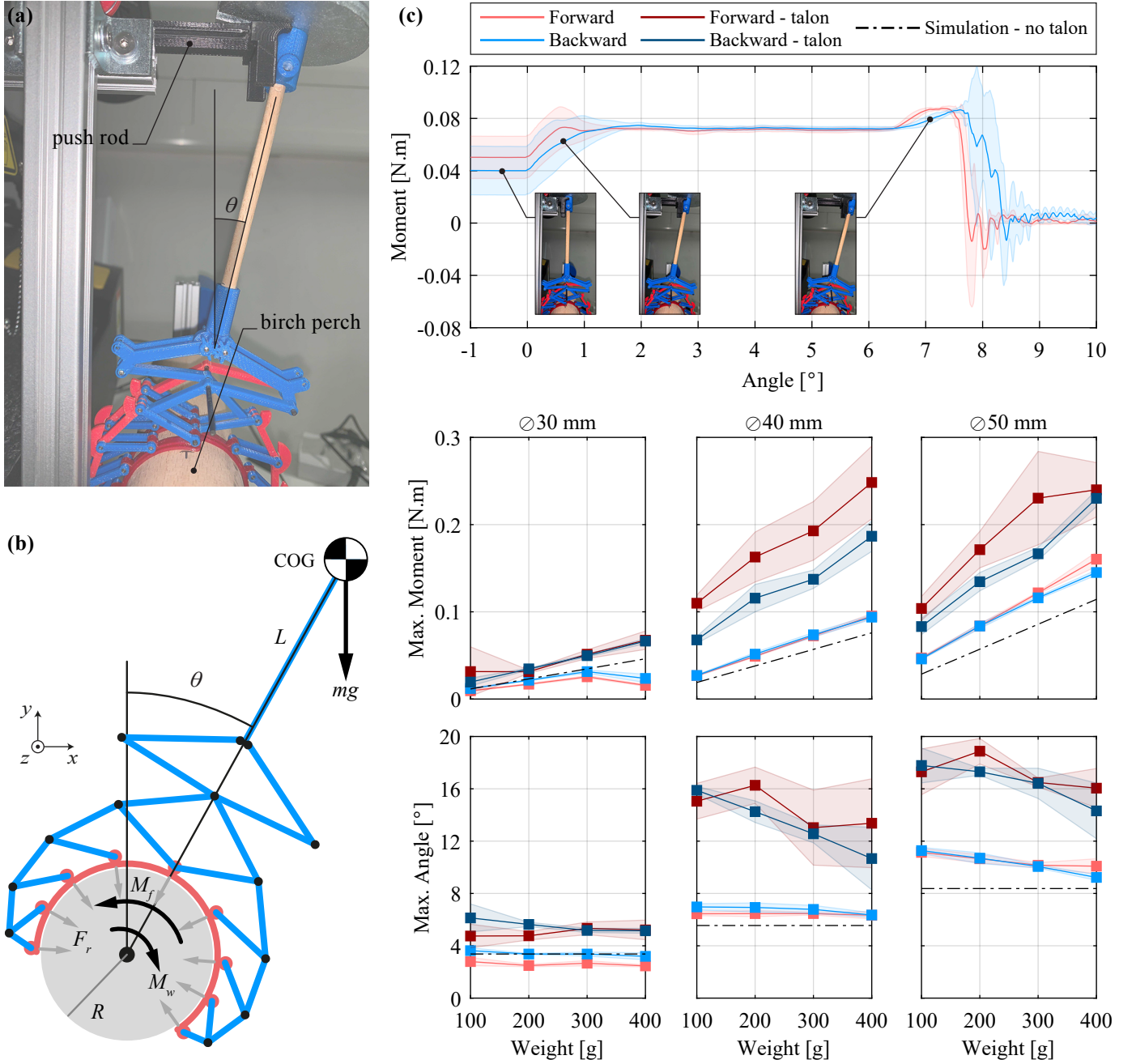
$\gamma = 110$ degrees being at only 35 degrees). The drawback is that the higher γ would limit the hyperextended stretching (notice that the red line in Fig. 2c cannot even reach the hyperextended state), which is required for walking. On the other hand, decreasing γ would allow for more hyperextended stretching, but would limit the range of perching diameters.

A single 10.2 cm long claw and Hoberman leg weighs only 23 g. When servos, leg linkages, and a controller are added to the leg to enable walking, the total weight goes up to 57 g. The claws are used as a pair, so the whole system comes to 114 g. This is considerably lighter than the designs by Doyle and Nandan (478 g and 178 g, respectively) [1], [30].

IV. PERCHING CHARACTERIZATION

Variations in the perching approach and maneuver can lead to the UAV tilted to one side of the perch. To be robust while perching, the claw must maintain its grip even when the UAV is tilted. We characterized this robustness by measuring the squeezing force a single claw can exert, how far the UAV can tilt before falling, and how much torque the claw can exert before slipping. We also demonstrated the robust perching in flight with a UAV equipped with a set of two claws.

To measure the squeezing force of the claw, we used a split perch setup similar to the one in [18]. We found that the squeezing force is directly proportional to body weight and perch diameter (Fig. 3c). This matches the predictions of the analysis of the Hoberman linkage (Fig. 2c), which indicate that the force imparted on the Fin Ray[®] device by the Hoberman linkage increases with increasing perch diameter. For comparison, this trend of lower squeezing forces on smaller diameter perches is the opposite of what was found by Roderick et al. [18], who noted that the birds squeezed harder on smaller perches. Furthermore, the birds could squeeze up



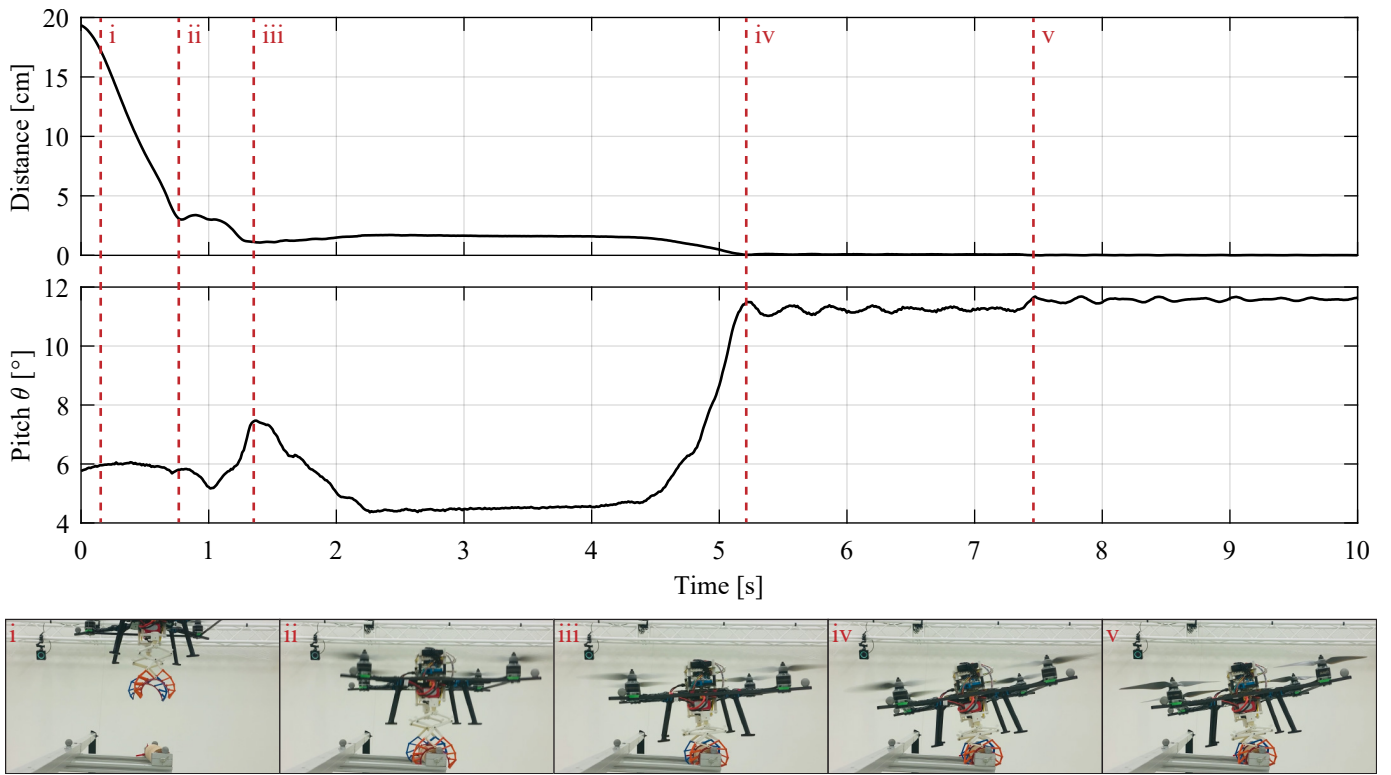


Fig. 5. Perching experiment with a manually piloted quadcopter equipped with a set of two claws. Plots show the vertical distance from the perch and the tilting (pitch) angle over time. The snapshots from the video correspond to different instances of the perching maneuver. Instant (i) shows the UAV in flight before the touchdown, and (ii) is when it makes contact with the wooden perch. Instant (iii) highlights when the claws are fully closed and firmly grip the perch. The drop in the vertical distance indicates this behavior. The back-and-forth shift in the pitch is due to the unbalanced thrust from the propellers during the process of slowly cutting off the thrust. The UAV tilts back when the thrust is significantly reduced, as shown at instant (iv). Finally, when the propellers are completely stopped (v), the UAV still remains perched, resting with a pitch angle of 11.6 degrees.

to two times their body weight. The maximum normalized squeezing force generated by the passive claw was just over one, with 100 g of weight on the 50 mm perch. Reaching a squeezing force comparable to the birds would require either the addition of actuators or modifying the Hoberman link to provide more mechanical advantage.

The results of the squeezing force characterization are compared to a static force model, detailed in Supplementary Text. The assumptions made in modeling the claw prove reasonable, as the model predicts well the trends in the experimental results (Fig. 3c). In addition, it correctly estimates that the increase in squeezing force from 40 mm to 50 mm is less than the increase in squeezing force from 30 mm to 40 mm. However, the prototype claw overperforms the model at lower weights, especially for the 50 mm perch. Under these lower weights, the claw experiences less deformation in the toe pad and does not perfectly conform to the shape of the perch, which is explicitly not accounted for in the model.

We investigated how far off-center the claw can reach before slipping by setting up a benchtop test apparatus to measure the maximum sustainable angle and corresponding moment (Fig. 4a). Representative moment data from one of the experiments is shown in Fig. 4c alongside predictions from the previously used static force model, detailed in Supplementary Text. There are three main phases of the test. In the beginning, the wooden rod is vertical, and the push rod is not in contact with the

wooden rod. At $\theta = 0$, the push rod comes into contact with the wooden rod, marking the beginning of the second phase. In this phase, the wooden rod is pushed, and the moment increases. During this phase, static friction holds the claw in position against the increasing moment. The measured increase in θ during this period results from the claw deforming. At about 2 degrees, the moment levels off and remains constant. During this phase, the claw is slipping, and dynamic friction is holding the claw on the perch. Once the claw reaches about 6.5 degrees, the moment due to the weight begins increasing again. Lastly, there is a sharp drop in the moment as the claw finally slips, and just before 8 degrees, the wooden rod falls and hits a catch.

Increasing the weight causes a greater measured moment before slipping, as expected based on the results of the squeezing test (Fig. 4c). However, the maximum angle is less affected by weight change and remains almost constant. The claw performs better on larger perch sizes due to increased squeezing force with perch diameter. The model predicts these trends well but with minor errors attributable to decreasing model accuracy at lower weights, as previously discussed. Unlike squeezing force experiments, the forces at the joints of the forward and backward digits differ in the tilting tests. At its current state, the claw can sustain weights up to 400 g (corresponding to twenty times its own weight). The 3D-printed joints and the claw would require reinforcement and design optimization to

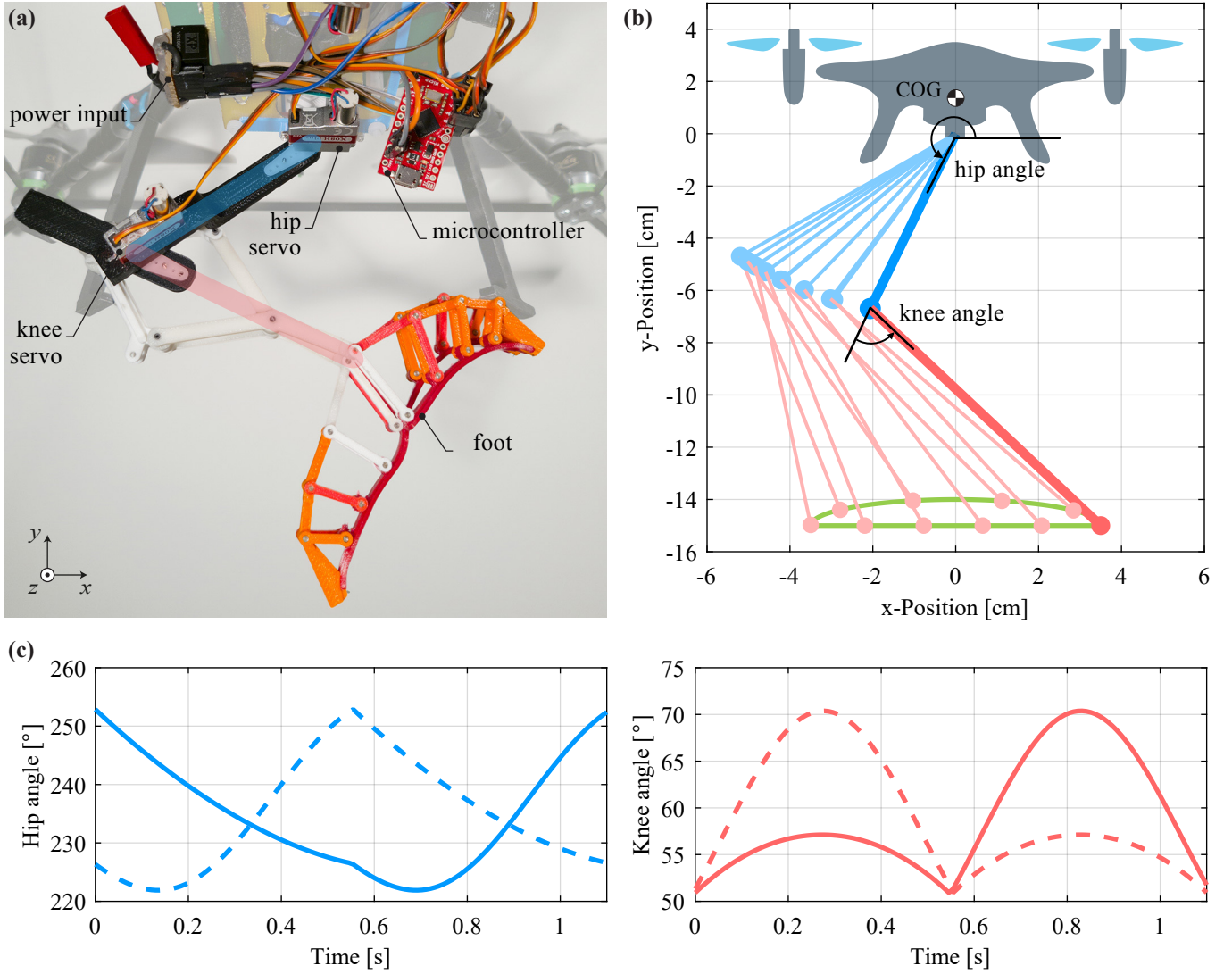


Fig. 6. (a) Close-up picture of the leg and walking control system. (b) Leg and foot trajectories, illustrating the positions of the upper limb, lower limb, and foot for a walking cycle. The UAV is not drawn to scale. (c) Joint angles for the hip and knee joints. Solid and dashed lines represent left and right leg trajectories with a 50% duty cycle phase difference.

reach weights beyond this point. With the addition of talons to the claw, there is a considerable increase (50-150%) in the achievable angle. However, it comes with an increase in variability between runs. This is due to the talons getting caught in asperities, which are randomly dispersed in the grain of the wooden perch.

A custom-built, manually controlled quadcopter UAV was equipped with two claws with talons, weighing 700 g in total. To demonstrate perching in action, we conducted four experiments with the UAV taking off from the ground, briefly flying around, and carefully landing on a 50 mm diameter birch perch. The UAV successfully perched in three trials, only losing balance once due to a high tilting angle resulting from a correspondingly high approach angle. Figure 5 shows representative data from a successful perching trial. It also presents data on vertical distance (altitude) from the perch, the pitch angle (corresponding to θ in Fig. 4a-b), and snapshots of notable events during the perching maneuver. The experiments

were carried out indoors, and the data were collected using an OptiTrack motion capture system. We also investigated the limits of UAV tilting. To do this, the UAV was set on the perch and slowly pushed by hand until it fell off. After conducting the test 10 times, the UAV slipped at an average of 19.4 degrees with a standard deviation of 0.65 degrees.

V. LEGGED LOCOMOTION CHARACTERIZATION

To demonstrate the stable walking ability of the proposed leg and claw system, we added actuation to the claws attached to the quadcopter used for the perching experiment (Fig. 6a). For each leg, two servo motors (KST X08), located directly at the joints, drive the hip and knee joints. The upper and lower limb lengths are 7 cm and 10 cm, respectively. The lower limb length, determined considering the torque limitation of the servo motors, cannot be shorter than 10 cm due to the length of the Hoberman linkage and the claw. The distance between the two legs is 10.5 cm. The walking gait is generated

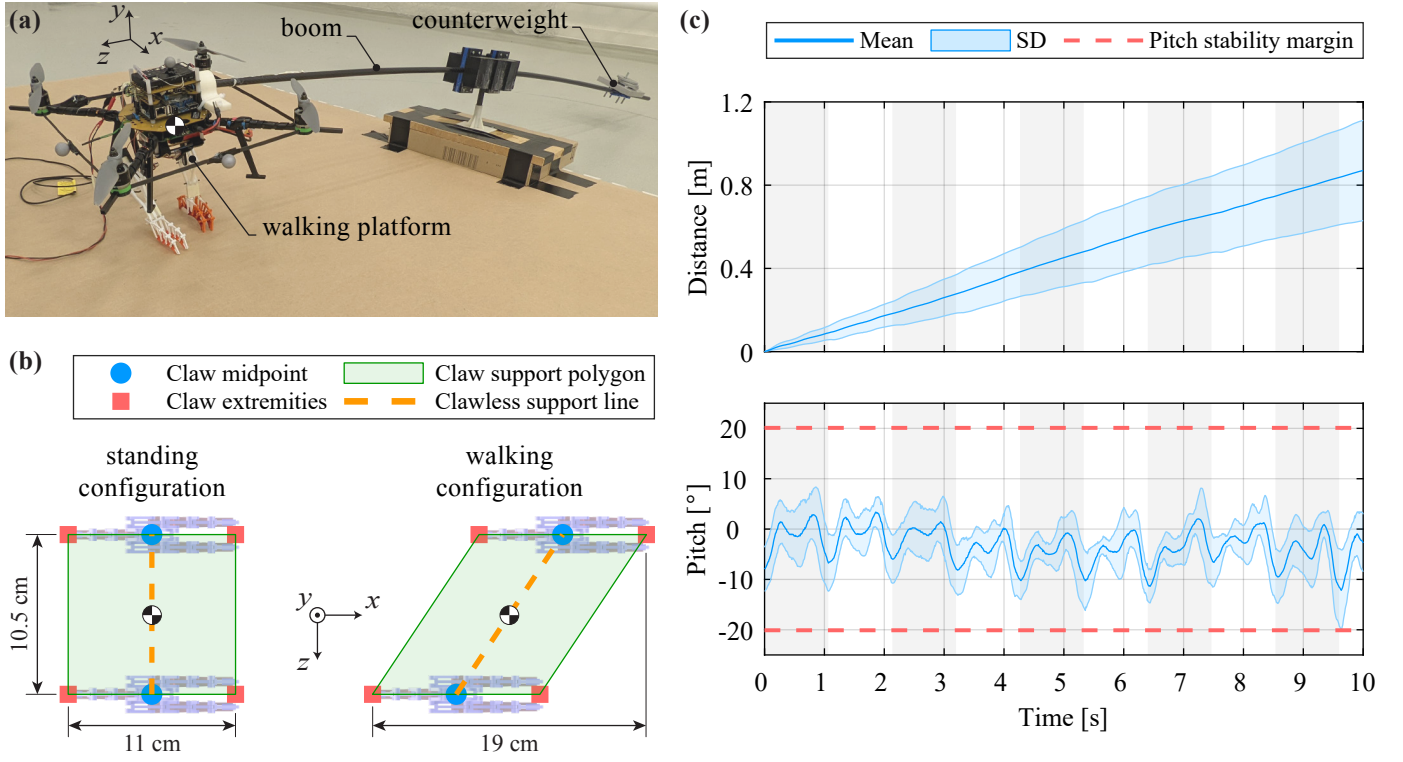


Fig. 7. (a) Image of the walking experimental setup. (b) Support polygons with hyperextended claws. (c) Distance traveled and pitch angle data of walking experiments with the hyperextended feet. The grey-shaded regions represent the left or right claw stance phases. In (b), the left is when the two feet are stretched out to the maximum separation distance, and the right is when the legs are in a natural standing position. The hyperextended claws expand the support polygon by providing extra contact points at the tips of the claws.

by a position control method following a half ellipse trajectory as shown in Fig. 6 with a phase difference of 50%. The flat trajectory is to provide a flat center of gravity (COG) forward movement when the foot is in contact with the ground, and the arc trajectory is to retract the leg without touching the ground. A Sparkfun Pro Micro board maps the half ellipse trajectory to the angular position values and commands the servo motors to follow the given angular position values.

The claw design can provide a stable gait for a bipedal system when the claw is in the hyperextended mode. The hyperextended feet provide extra contact points with the ground and, consequently, enlarge the support polygon (Fig. 7b). Fig. 7 shows the region of support polygon formed by the extremities of the claws when both legs are on the ground. The left and right diagrams present the support polygons when the legs are in a neutral position and when the legs are fully stretched forward and backward, respectively. The orange dashed lines indicate where the center of gravity would need to be located in the absence of the claws if the legs were point feet. With a stride length of 8 cm, the support polygon changes from a rectangular stance area of 99.75 cm^2 to a parallelogram of 115.5 cm^2 during walking.

The robotic platform was connected to a boom support system and walked around a pivot axis in a circular trajectory (Fig. 7). The boom system was installed for two reasons. The servo motors provide degrees of freedom only in the sagittal plane. Thus, the current setup could only provide stability in pitch angle. Another reason was to reduce the resultant

weight with a counterweight due to the power limitation of the servo motors that drove the leg mechanism. The position and orientation of the robot were collected using an OptiTrack motion capture system to evaluate whether the claws' hyperextended configuration can provide stable terrestrial locomotion. Five walking trials were recorded at 120 Hz. On the other end of the boom, weights were installed to counterbalance the system, and the resultant effective weight of the system was 200 g. The distance traveled data are presented in Fig. 7c. The platform covered 0.87 m in 10 seconds at 1.1 Hz of walking frequency with the hyperextended feet. It could not walk or even stand when the claws were closed due to the limited support polygon area. Figure 7c also presents the pitch angle data during the walking, which shows a repeating pattern for each step. The pitch angle started around -8 degrees and had two local maximums of around 0 degrees for each step. This pattern was repeatedly shown for every one-second-long step, and the average pitch stayed around -5 degrees during the 10 seconds of walking. The pitch angle range did not diverge from the start of the experiment but stayed between -12 degrees and 5 degrees. The stability margin is calculated based on the center of gravity position and the support polygon size. It indicates the maximum pitch angle beyond which the robot tips over. The maximum allowed pitching angle of the platform was ± 20.1 degrees, and the platform stayed within this range throughout the experiment. These results indicate that the hyperextended configuration provides stable walking in pitch because the average pitch angle does not change

significantly in the 10 seconds of walking.

VI. CONCLUSIONS

The claws presented in this manuscript enable for the first time ever, passive perching, walking, and flying of a UAV. The lightweight construction of the Hoberman linkage legs and Fin Ray® claws are capable of holding up to a 700 g UAV. We have presented important sizing relationships and static models for calculating expected performance.

Although the claws developed here are completely passive, actuators could be used to further increase their squeezing force allowing them to be scaled up for use on heavier UAVs. These actuators would mimic the muscles that birds use to grasp perches. Future iterations could also include actuators to automatically switch leg modes between walking and perching.

These claws widen the range of possibilities of multimodal UAVs by enabling walking and perching. In particular, the use of these claws in semi- or fully-erect walking robots gives them advantages over sprawling or wheeled alternatives in navigating cluttered environments. This is because their longer legs are able to stride over larger obstacles. The perching capability allows them to remain in position for long periods of time to recharge batteries, conduct observations, or minimize noise and power consumption. This will lead to future robots with a larger range of capabilities, making them more versatile tools for search and rescue operations.

VII. ACKNOWLEDGEMENTS

The authors are grateful for the engineering help provided by Olexandr Gudozhnik, the useful feedback from Florian Achermann, and the piloting skills of Przemyslaw Kornatowski and Victor Casas Rochel.

REFERENCES

- [1] C. E. Doyle, J. J. Bird, T. A. Isom, J. C. Kallman, D. F. Bareiss, D. J. Dunlop, R. J. King, J. J. Abbott, and M. A. Minor, "An Avian-Inspired Passive Mechanism for Quadrotor Perching," *IEEE/ASME Transactions on Mechatronics*, vol. 18, no. 2, pp. 506–517, Apr. 2013.
- [2] M. Tieu, D. M. Michael, J. B. Pflueger, M. S. Sethi, K. N. Shimazu, T. M. Anthony, and C. L. Lee, "Demonstrations of Bio-Inspired Perching Landing Gear for UAVs," in *Proc. SPIE 9797, Bioinspiration, Biomimetics, and Bioreplication 2016*, 2016.
- [3] A. McLaren, Z. Fitzgerald, G. Gao, and M. Liarokapis, "A Passive Closing, Tendon Driven, Adaptive Robot Hand for Ultra-Fast, Aerial Grasping and Perching," in *2019 IEEE/RSJ International Conference on Intelligent Robots and Systems (IROS)*, Nov. 2019, pp. 5602–5607.
- [4] M. T. Pope, C. W. Kimes, H. Jiang, E. W. Hawkes, M. A. Estrada, C. F. Kerst, W. R. T. Roderick, A. K. Han, D. L. Christensen, and M. R. Cutkosky, "A Multimodal Robot for Perching and Climbing on Vertical Outdoor Surfaces," *IEEE Transactions on Robotics*, vol. 33, no. 1, pp. 38–48, Dec. 2016.
- [5] E. W. Hawkes, D. L. Christensen, E. V. Eason, M. A. Estrada, M. Heverly, E. Hilgemann, H. Jiang, M. T. Pope, A. Parness, and M. R. Cutkosky, "Dynamic Surface Grasping with Directional Adhesion," in *2013 IEEE/RSJ International Conference on Intelligent Robots and Systems*, 2013, pp. 5487–5493.
- [6] H. Jiang, M. T. Pope, E. W. Hawkes, D. L. Christensen, M. A. Estrada, A. Parlier, R. Tran, and M. R. Cutkosky, "Modeling the dynamics of perching with opposed-grip mechanisms," in *2014 IEEE International Conference on Robotics and Automation (ICRA)*, May 2014, pp. 3102–3108.
- [7] M. A. Graule, P. Chirarattananon, S. B. Fuller, N. T. Jafferis, K. Y. Ma, M. Spenko, R. Kornbluh, and R. J. Wood, "Perching and Takeoff of a Robotic Insect on Overhangs Using Switchable Electrostatic Adhesion," *Science*, vol. 352, no. 6288, pp. 978–982, 2016.
- [8] K. Hang, X. Lyu, H. Song, J. A. Stork, A. M. Dollar, D. Kragic, and F. Zhang, "Perching and resting—a paradigm for uav maneuvering with modularized landing gears," *Science Robotics*, vol. 4, no. 28, p. eaau6637, 2019.
- [9] K. Zhang, P. Chermprayong, T. M. Alhinai, R. Siddall, and M. Kovac, "SpiderMAV: Perching and Stabilizing Micro Aerial Vehicles with Bio-Inspired Tensile Anchoring Systems," in *2017 IEEE/RSJ International Conference on Intelligent Robots and Systems (IROS)*, Sep. 2017, pp. 6849–6854.
- [10] H.-N. Nguyen, R. Siddall, B. Stephens, A. Navarro-Rubio, and M. Kováč, "A Passively Adaptive Microspine Grapple for Robust, Controllable Perching," in *2019 2nd IEEE International Conference on Soft Robotics (RoboSoft)*, Apr. 2019, pp. 80–87.
- [11] Y. H. Hsiao and P. Chirarattananon, "Ceiling Effects for Hybrid Aerial–Surface Locomotion of Small Rotorcraft," *IEEE/ASME Transactions on Mechatronics*, vol. 24, no. 5, pp. 2316–2327, Oct. 2019.
- [12] W. Stewart, E. Ajanic, M. Müller, and D. Floreano, "How to swoop and grasp like a bird with a passive claw for a high-speed grasping," *IEEE/ASME Transactions on Mechatronics*, vol. 27, no. 5, pp. 3527–3535, 2022.
- [13] W. Stewart, L. Guarino, E. Piskarev, and D. Floreano, "Passive Perching with Energy Storage for Winged Aerial Robots," *Advanced Intelligent Systems*, vol. In Review, 2021.
- [14] D. Mehanovic, J. Bass, T. Courteau, D. Rancourt, and A. Lussier Desbiens, "Autonomous Thrust-Assisted Perching of a Fixed-Wing UAV on Vertical Surfaces," in *Biomimetic and Biohybrid Systems*, ser. Lecture Notes in Computer Science, M. Mangan, M. Cutkosky, A. Mura, P. F. Verschure, T. Prescott, and N. Lepora, Eds. Cham: Springer International Publishing, 2017, pp. 302–314.
- [15] M. Anderson, "The Sticky-Pad Plane and Other Innovative Concepts for Perching UAVs," in *47th AIAA Aerospace Sciences Meeting Including The New Horizons Forum and Aerospace Exposition*, 2009.
- [16] H. Hsiao, J. Sun, H. Zhang, and J. Zhao, "A mechanically intelligent and passive gripper for aerial perching and grasping," *IEEE/ASME Transactions on Mechatronics*, vol. 27, no. 6, pp. 5243–5253, 2022.
- [17] M. A. Daley and A. A. Biewener, "Running over rough terrain reveals limb control for intrinsic stability," *Proceedings of the National Academy of Sciences*, vol. 103, no. 42, pp. 15 681–15 686, 2006.
- [18] W. R. Roderick, D. D. Chin, M. R. Cutkosky, and D. Lentink, "Birds land reliably on complex surfaces by adapting their foot-surface interactions upon contact," *eLife*, vol. 8, p. e46415, Aug. 2019.
- [19] C. J. Pratt and K. K. Leang, "Dynamic underactuated flying-walking (DUCK) robot," in *2016 IEEE International Conference on Robotics and Automation (ICRA)*, May 2016, pp. 3267–3274.
- [20] K. Kim, P. Spieler, E.-S. Lupu, A. Ramezani, and S.-J. Chung, "A bipedal walking robot that can fly, slackline, and skateboard," *Science Robotics*, vol. 6, no. 59, p. eabf8136, Oct. 2021.
- [21] O. Pfaff, S. Simeonov, I. Cirovic, P. Stano *et al.*, "Application of fin ray effect approach for production process automation," *Annals of DAAAM & Proceedings*, vol. 22, no. 1, pp. 1247–1249, 2011.
- [22] W. D. Shin, J. Park, and H.-W. Park, "Development and experiments of a bio-inspired robot with multi-mode in aerial and terrestrial locomotion," *Bioinspiration & Biomimetics*, vol. 14, no. 5, p. 056009, Jul. 2019.
- [23] L. Daler, S. Mintchev, C. Stefanini, and D. Floreano, "A bioinspired multi-modal flying and walking robot," *Bioinspiration & Biomimetics*, vol. 10, no. 1, p. 016005, Jan. 2015.
- [24] F. Boria, R. Bachmann, P. Ifju, R. Quinn, R. Vaidyanathan, C. Perry, and J. Wagener, "A sensor platform capable of aerial and terrestrial locomotion," in *2005 IEEE/RSJ International Conference on Intelligent Robots and Systems*, Aug. 2005, pp. 3959–3964.
- [25] A. Kalantari and M. Spenko, "Design and experimental validation of HyTAQ, a Hybrid Terrestrial and Aerial Quadrotor," in *2013 IEEE International Conference on Robotics and Automation*, May 2013, pp. 4445–4450.
- [26] H. Wang, J. Shi, J. Wang, H. Wang, Y. Feng, and Y. You, "Design and Modeling of a Novel Transformable Land/Air Robot," *International Journal of Aerospace Engineering*, vol. 2019, p. e2064131, Feb. 2019.
- [27] R. Käsliin, H. Kolvenbach, L. Paez, K. Lika, and M. Hutter, "Towards a passive adaptive planar foot with ground orientation and contact force sensing for legged robots," in *2018 IEEE/RSJ International Conference on Intelligent Robots and Systems (IROS)*, IEEE, 2018, pp. 2707–2714.
- [28] F. B. Gill, *Ornithology*, 3rd ed. New York: W.H. Freeman, 2007.
- [29] P. M. Galton and J. D. Shepherd, "Experimental analysis of perching in the european starling (*sturnus vulgaris*: Passeriformes; passerines), and the automatic perching mechanism of birds," *Journal of Experimental Zoology Part A: Ecological Genetics and Physiology*, vol. 317, no. 4, pp. 205–215, 2012.

- [30] P. M. Nadan, T. M. Anthony, D. M. Michael, J. B. Pflueger, M. S. Sethi, K. N. Shimazu, M. Tieu, and C. L. Lee, "A bird-inspired perching landing gear system," *Journal of Mechanisms and Robotics*, vol. 11, no. 6, 2019.
- [31] W. Chi, K. H. Low, K. H. Hoon, J. Tang, and T. H. Go, "A bio-inspired adaptive perching mechanism for unmanned aerial vehicles," *Journal of Robotics and Mechatronics*, vol. 24, no. 4, pp. 642–648, 2012.
- [32] X. Shan and L. Birglen, "Modeling and analysis of soft robotic fingers using the fin ray effect," *The International Journal of Robotics Research*, vol. 39, no. 14, pp. 1686–1705, 2020.
- [33] C. I. Basson and G. Bright, "Geometric conformity study of a fin ray gripper utilizing active haptic control," in *2019 IEEE 15th International Conference on Control and Automation (ICCA)*. IEEE, 2019, pp. 713–718.
- [34] K. Elgeneidy, P. Lightbody, S. Pearson, and G. Neumann, "Characterising 3d-printed soft fin ray robotic fingers with layer jamming capability for delicate grasping," in *2019 2nd IEEE International Conference on Soft Robotics (RoboSoft)*. IEEE, 2019, pp. 143–148.
- [35] E. Culler, G. Thomas, and C. Lee, "A perching landing gear for a quadcopter," in *53rd AIAA/ASME/ASCE/AHS/ASC Structures, Structural Dynamics and Materials Conference 20th AIAA/ASME/AHS Adaptive Structures Conference 14th AIAA*, 2012, p. 1722.
- [36] W. Crooks, S. Rozen-Levy, B. Trimmer, C. Rogers, and W. Messner, "Passive gripper inspired by manduca sexta and the fin ray® effect," *International Journal of Advanced Robotic Systems*, vol. 14, no. 4, p. 1729881417721155, 2017.
- [37] K. C. V. Broers and S. F. Armanini, "Design and Testing of a Bioinspired Lightweight Perching Mechanism for Flapping-Wing MAVs Using Soft Grippers," *IEEE Robotics and Automation Letters*, vol. 7, no. 3, pp. 7526–7533, Jul. 2022.
- [38] M. L. Burroughs, K. Beauwen Freckleton, J. J. Abbott, and M. A. Minor, "A sarrus-based passive mechanism for rotorcraft perching," *Journal of Mechanisms and Robotics*, vol. 8, no. 1, 2016.
- [39] C. Hoberman, "Radial expansion/retraction truss structures," US Patent US5 024 031A, Jun., 1991.
- [40] A. S. Mata, A. B. Torras, J. A. C. Carrillo, F. E. Juanco, A. J. G. Fernández, F. N. Martínez, and A. O. Fernández, *Fundamentals of machine theory and mechanisms*. Springer, 2016, vol. 40.



Mohammad Askari received the B.S. (2015) and M.S. (2018) degrees, both with the highest distinction, in mechanical engineering from Middle East Technical University and Bilkent University in Ankara, Turkey, respectively. From 2015 to 2019, he was with the Bilkent Miniature Robotics Laboratory, where he worked on origami-inspired miniature walking robots. Since 2020, he has been with the Laboratory of Intelligent Systems at École Polytechnique Fédérale de Lausanne (EPFL), Lausanne, Switzerland. His current research interests include

mechanical design, dynamics and control, flight mechanics, and aerial robotics.



Won Dong Shin received the B.S. and M.S. degrees in mechanical engineering from the University of Illinois at Urbana-Champaign, Champaign, IL, USA, in 2016 and 2018, respectively. Since 2019, he has been working toward the Ph.D. degree in robotics with the Laboratory of Intelligent Systems, École Polytechnique Fédérale de Lausanne, Lausanne, Switzerland.



William Stewart (Member, IEEE) received the M.S. and Ph.D. degrees in aerospace engineering from North Carolina (NC) State University, Raleigh, NC, USA, in 2014, and 2018, respectively. From 2010 to 2014, he was a leader of the NC State University Aerial Robotics Team. From 2014 to 2016, he worked as a Research Assistant on the Eagle Ray project with the Smart Composites Laboratory. Since 2018, he has worked as a Postdoctoral Researcher with the Laboratory of Intelligent Systems, Swiss Federal Institute of Technology Lausanne (EPFL), Lausanne, Switzerland. His research interests include aerodynamics, mechanics, and vehicle design. Dr. Stewart was two-time AUVSI student UAS competition champion (2010 and 2014).



Damian Lenherr received the B.S. and M.S. degrees in mechanical engineering from the Swiss Federal Institute of Technology in Zurich (ETHZ), Zurich, Switzerland, in 2019 and 2021, respectively. In the context of a student exchange during the spring semester of 2021, he has been working on his master's thesis with the Laboratory of Intelligent Systems at École Polytechnique Fédérale de Lausanne (EPFL), Lausanne, Switzerland.



Dario Floreano (Fellow, IEEE) received the M.A. degree in vision psychophysics from Univ. Trieste, Italy, in 1988, the M.S. degree in neural computation from Univ. Stirling, UK, in 1992, and the Ph.D. degree in robotics from Univ. Trieste, Italy, in 1995.

He is a full Professor and director of the Laboratory of Intelligent Systems, Swiss Federal Institute of Technology Lausanne (EPFL), Lausanne, Switzerland. He has been the Founding Director of the Swiss National Center of Competence in Robotics between 2010 and 2022. He held visiting fellowships with

Sony Computer Science Laboratory, Tokyo, Japan; Caltech/JPL, Pasadena, CA, USA; and Harvard University, Boston, MA, USA. His research interests include biologically inspired robotics and artificial intelligence. He has made pioneering contributions to the fields of evolutionary robotics, aerial robotics, and soft robotics. He spun off two robotics companies: senseFly (2009, acquired by the Parrot Group in 2016), which has become a world leader in drones for agriculture and imaging, and Flyability (2015), which is the world leader in inspection drones for confined spaces. In 2017, the Economist dedicated a center page portrait to Prof. Floreano (Brain Scan).

Prof. Floreano joined the Advisory Board of the Future and Emerging Technologies division of the European Commission, served as Vice-Chair of the World Economic Forum Agenda Council on Smart Systems and Robotics, has been a co-founder of the International Society of Artificial Life, elected member of the Board of Governors of the International Neural Network Society. He is on the advisory board of several institutes and international organizations in robotics and artificial intelligence, and served on the editorial board of several scientific journals. He is a Fellow of the IEEE Society and the ELLIS society.

Supplementary Test

PERCHING MODEL

In modeling the claw for perching (Fig. S1), we make the following assumptions:

- 1) Under any payload, the claw's soft sole (red toe pad) conforms to the shape of the perch of any size and is in perfect contact with it.
- 2) Due to the claw's planar symmetry, we only consider modeling the linkage on one side. Furthermore, the payload is assumed to be split equally between the two sides.
- 3) The claw in perched configuration is treated as a fully rigid system with negligible weight. This means that all the comprising links, including the soft toe pad, are assumed to be rigid and weightless.
- 4) The model does not include the talons and only predicts the talon-less claw type.

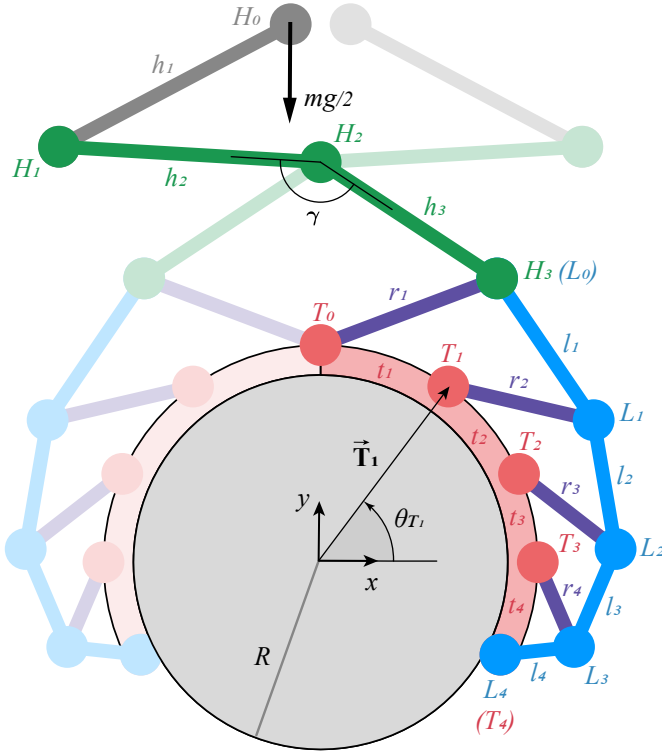


Fig. S1. Schematic diagram of the claw in perched configuration. Capital letters denote the joint names, and lowercase letters the corresponding link lengths of the Hoberman linkage (H, h), toe pad (T, t), outer-links (L, l), and ribs (r). Throughout the section, a vector notation represents the position vector to a joint with its angle denoted by the θ symbol preceding the joint name. An example is shown for T_1 .

A. Kinematic Analysis

For a given perch radius of R , we first solve for all the joint locations in perched configuration. The position vector of the toe pad joints are found by:

$$\vec{T}_i = R [\cos \theta_{T_i} \quad \sin \theta_{T_i} \quad 0]^T,$$

$$\text{where } \theta_{T_i} = \frac{\pi}{2} - \frac{1}{R} \sum_{j=0}^i t_j.$$

In the above equations, i is the subscript number of the toe pad joint ($i = 0$ to 4), and θ_{T_i} represents the angle of the position vector from horizontal. If we calculate and denote the angle of $(\vec{T}_4 - \vec{T}_3)$ vector by θ_{t_4} , the position of joint T_3 can be found using the cosine law for triangle $T_3T_4L_3$ as follows:

$$\vec{L}_3 = \vec{T}_3 + r_4 [\cos(\theta_{t_4} + \alpha) \quad \sin(\theta_{t_4} + \alpha) \quad 0]^T,$$

$$\text{where } \alpha = \arccos \frac{t_4^2 + r_4^2 - l_4^2}{2t_4r_4}.$$

The rest of the Fin Ray[®] linkage has three interdependent four-bars, the kinematic solution of which can yield the position of the remaining outer-link joints (L_2 , L_1 , and L_0).

These four-bar linkages are $T_2T_3L_3L_2$, $T_1T_2L_2L_1$, and $T_0T_1L_1L_0$. We skip here detailed derivation of these joint locations for brevity and present only the method used to solve the four-bar kinematics in the following section.

Having determined all the joint locations of the outer-links, we can solve for the Hoberman joints as follows:

$$\vec{H}_2 = [0 \quad L_{3y} + \sqrt{h_3^2 - L_{0x}^2} \quad 0]^T,$$

$$\vec{H}_1 = \vec{H}_2 + h_2 [\cos(\theta_{h_3} - \gamma) \quad \sin(\theta_{h_3} - \gamma) \quad 0]^T,$$

$$\vec{H}_0 = [0 \quad H_{1y} + \sqrt{(h_1^2 - (H_{0x} - H_{1x})^2)} \quad 0]^T,$$

where θ_{h_3} is the angle of $(\vec{H}_3 - \vec{H}_2)$ vector relative to positive x axis, $\gamma = 150^\circ$ is the fixed Hoberman angle from Fig. 2, and H_{0x} is the fixed horizontal distance corresponding to the radius of the gear at the H_0 joint.

B. Four-bar Position Kinematics

The position analysis of four-bar mechanisms generally consists of nonlinear equations, which can be computationally challenging or slow to solve. This nonlinearity arises due to the existence of multiple solutions (Fig. S2). We propose here a unique position analysis method, applicable to any four-bar mechanism, to avoid solving any nonlinearity. The solution presented here is based on the method proposed by [40].

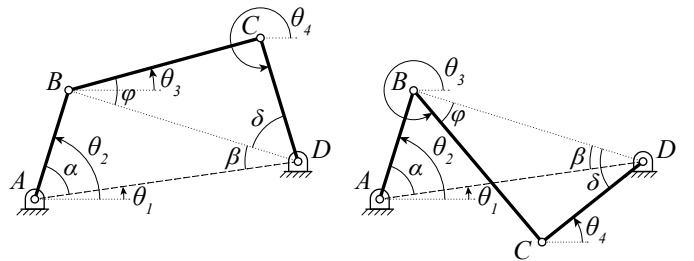


Fig. S2. The possible solutions for a generic four-bar mechanism with fixed pivots at A and D: open configuration (left) and crossed configuration (right).

For any given crank input (θ_2) to a generic four-bar mechanism shown in Fig. S2, with known link lengths and fixed pivot positions of A and D, we can solve for the unknown coupler and rocker angles, θ_3 and θ_4 , respectively, as follows:

$$\begin{aligned}\alpha &= \theta_2 - \theta_1, \\ \overline{BD} &= \sqrt{\overline{AB}^2 + \overline{AD}^2 - 2\overline{AB}\overline{AD}\cos\alpha}, \\ \beta &= \text{atan2}(\sin\beta, \cos\beta), \\ \text{where,} \\ \sin\beta &= \frac{\overline{AB}}{\overline{BD}}\sin\alpha \quad \text{and} \quad \cos\beta = \frac{\overline{AD}^2 + \overline{BD}^2 - \overline{AB}^2}{2\overline{AD}\overline{BD}}.\end{aligned}$$

$$\begin{aligned}\text{Similarly,} \\ \phi &= \arccos\left(\frac{\overline{BC}^2 + \overline{BD}^2 - \overline{CD}^2}{2\overline{BC}\overline{BD}}\right), \\ \delta &= \text{atan2}(\sin\delta, \cos\delta), \\ \text{where,}\end{aligned}$$

$$\sin\delta = \frac{\overline{BC}}{\overline{CD}}\sin\phi \quad \text{and} \quad \cos\delta = \frac{\overline{BD}^2 + \overline{CD}^2 - \overline{BC}^2}{2\overline{BD}\overline{CD}}.$$

Then the solutions to the two possible configurations of a four-bar are given by:

$$\begin{aligned}\text{Open configuration: } & \begin{cases} \theta_3 = \theta_1 - \beta + \phi, \\ \theta_4 = \theta_1 - \beta - \delta, \end{cases} \\ \text{Crossed configuration: } & \begin{cases} \theta_3 = \theta_1 - \beta - \phi, \\ \theta_4 = \theta_1 - \beta + \delta. \end{cases}\end{aligned}$$

Note that $\text{atan2}(y, x)$ in the above equations is the four-quadrant inverse tangent function of the two variables x and y , i.e., $\arctan(x/y)$.

C. Static Force Equilibrium

Following the kinematic analysis of the claw in perched configuration, a static force balance is carried out. Doing so can resolve the internal forces at each joint based on the input payload. The horizontal components of the resolved forces at the toe pad joints (T_1 through T_4 in Fig. S1) can then be compared to the split perch test results for validation.

A total of 40 unknown forces are considered when formulating the linear system of equations. We place two reaction forces at joints connected by two links or less and six reaction forces for those connected by three links (L_0 through L_3), i.e., two forces per each of the three links. Hence, a minimum of 40 equations are needed to resolve these forces. Note that enforcing a two-force member assumption can greatly reduce the number of unknowns. Except for the Hoberman link, which has three joints, all the links are under compression or tension. Hence the resultant reaction forces at their joints are colinear, i.e., being a two-force member. However, we do not enforce this and instead use it as a tool to verify whether the more general

approach satisfies the two-force member assumption once solved. 33 equations come from force and moment balance about the 11 rigid links in the system (including the whole toe pad as one link). The remaining (8 equations) come from a force equilibrium constraint at the outer wall joints connected by three links, resulting in a total of 41 equations. For brevity, we do not derive the entire system of equations here and present only a few examples for the Hoberman links and outer-link joint L_0 . If we define moment(\vec{r}, \vec{F}) as the z-component of the cross product of $\vec{r} \times \vec{F}$, then we have from force equilibrium of h_1 link:

$$\begin{aligned}\text{eqn1: } & +F_{H_{0x}} + F_{H_{1x}} = 0, \\ \text{eqn2: } & +F_{H_{0y}} + F_{H_{1y}} - mg/2 = 0, \\ \text{eqn3: } & \text{moment}(\vec{r}, [+F_{H_{1x}} \quad 0 \quad 0]^T) + \\ & \text{moment}(\vec{r}, [0 \quad +F_{H_{1y}} \quad 0]^T) = 0, \\ \text{where } & \vec{r} = \vec{H}_1 - \vec{H}_0.\end{aligned}$$

Similarly, the force equilibrium of h_2h_3 link yields:

$$\begin{aligned}\text{eqn4: } & -F_{H_{1x}} + F_{H_{2x}} + F_{H_{3x}} = 0, \\ \text{eqn5: } & -F_{H_{1y}} + F_{H_{2y}} + F_{H_{3y}} = 0, \\ \text{eqn6: } & \text{moment}(\vec{r}_1, [-F_{H_{1x}} \quad 0 \quad 0]^T) + \\ & \text{moment}(\vec{r}_1, [0 \quad -F_{H_{1y}} \quad 0]^T) + \\ & \text{moment}(\vec{r}_2, [+F_{H_{3x}} \quad 0 \quad 0]^T) + \\ & \text{moment}(\vec{r}_2, [0 \quad +F_{H_{3y}} \quad 0]^T) = 0, \\ \text{where } & \vec{r}_1 = \vec{H}_1 - \vec{H}_2 \quad \text{and} \quad \vec{r}_2 = \vec{H}_3 - \vec{H}_2.\end{aligned}$$

As an example of the force equilibrium constraint at outer wall joints with three connected links, we have at joint L_0 :

$$\begin{aligned}\text{eqn7: } & +F_{H_{3x}} + F_{L_{0x}}^{r_1} + F_{L_{0x}}^{l_0} = 0, \\ \text{eqn8: } & +F_{H_{3y}} + F_{L_{0y}}^{r_1} + F_{L_{0y}}^{l_0} = 0.\end{aligned}$$

The remaining static equilibrium equations can be derived with a similar approach. If we denote the vector of 40 unknown forces by \vec{x} , then we can formulate all equations as a linear system in the form: $\mathbf{A}\vec{x} = \vec{b}$. Note that \mathbf{A} is a 41×40 matrix, and \vec{b} a 41×1 vector of external forces (payload only in this case). Hence, the forces at the joints are found by $\vec{x} = \mathbf{A}^{-1}\vec{b}$, where \mathbf{A}^{-1} is the Moore-Penrose pseudoinverse of \mathbf{A} .

D. Squeezing Force Estimation

The claw can only press on the perch with the forces exerted by its toe pad joints. However, not all joints contribute to a squeezing force. To compare results with the split perch experiments, we estimate the total exerted squeezing force on one half of the perch by the toe pad using:

$$F_{sq} = \sum_{i=1}^n \hat{F}_{T_{ix}} ,$$

$$\text{where } \hat{F}_{T_{ix}} = \begin{cases} 0 & F_{T_{ix}} > 0 \\ |F_{T_{ix}}| & F_{T_{ix}} \leq 0 \end{cases} .$$

From the actual split perch experiments, we observed that the number of joints contributing to a squeezing force varies with the perch diameter. Therefore, a value of $n = 2, 3$, and 4 were used for the 30 mm, 40 mm, 50 mm perch, respectively.

E. Maximum Tilting Moment and Sustainable Angle

We estimate the maximum sustainable angle using an inverted pendulum model with friction. When perching at an angle, the weight of the UAV (mg in Fig. 4b) is off-centered and creates a moment (M_w), which tends to cause the claw to slip. At the maximum sustainable angle, this moment must be balanced with a moment from the friction between the toe pad of the claw and the perch surface (M_f). We take an iterative approach to find the maximum tilting angle. Assuming an initial angle of θ_a , the moment due to weight M_w can be calculated using the following relation:

$$M_w = (R + L)mg \sin \theta_a, \quad (2)$$

where R is the radius of the perch and L is the lever arm length from the center of gravity to the perch surface. To find the resisting moment due to friction, we need to find the forces at each toe pad joint of the tilted claw. The tilting causes an asymmetric behavior between the right and left digits. Therefore, the kinematic analysis and the static force equilibrium steps need to be repeated separately for the left and right digits with the assumed inclination angle of θ_a . This gives the forces in the xy Cartesian coordinates, which must be resolved into radial and tangential components. The radial (normal) components create friction between the toe pad and the perch. If we resolve and denote the radial components of the toe pad joints by $F_{T_{ir}}$, the total friction force and the opposing moment to weight can be estimated by:

$$M_f = R\mu F_r ,$$

$$F_r = \sum_{digit}^{l,r} \sum_{i=0}^4 \hat{F}_{T_{ir}} ,$$

$$\text{where } \hat{F}_{T_{ir}} = \begin{cases} F_{T_{ir}} & F_{T_{ir}} \geq 0 \\ 0 & F_{T_{ir}} < 0 \end{cases} .$$

In the above equations, i is the subscript number of the toe pad joint ($i = 0$ to 4), μ_s is the static coefficient of friction between the toe pad and perch, and l and r denote the left and right digits, respectively. The condition that yields the maximum sustainable angle is $M_w = M_f$. If there is a mismatch between the two opposing moments, the assumed tilting angle (θ_a) must be updated, and the steps are repeated to find the solution iteratively.